A Lagrangian analysis of a two-dimensional airfoil with vortex shedding

2008 J. Phys. A: Math. Theor. 41 344011

(http://iopscience.iop.org/1751-8121/41/34/344011)

IOP PUBLISHING JOURNAL OF PHYSICS A: MATHEMATICAL AND THEORETICAL

J. Phys. A: Math. Theor. **41** (2008) 344011 (22pp) doi:10.1088/1751-8113/41/34/344011

A Lagrangian analysis of a two-dimensional airfoil with vortex shedding

Doug Lipinski, Blake Cardwell and Kamran Mohseni

Department of Aerospace Engineering Sciences, University of Colorado, Boulder, CO 80309-0429, USA

E-mail: Mohseni@colorado.edu

Received 6 December 2007, in final form 22 May 2008
Published 11 August 2008
Online at stacks.iop.org/JPhysA/41/344011

Abstract

Using invariant material manifolds and flow topology, the flow behavior and structure of flow around a two-dimensional Eppler 387 airfoil is examined with an emphasis on vortex shedding and the time-dependent reattachment profile. The examination focuses on low Reynolds number ($Re = 60\,000$) flow at several angles of attack. Using specialized software, we identify invariant manifolds in the flow and use these structures to illuminate the process of vortex formation and the periodic behavior of the reattachment profile. Our analysis concludes with a topological view of the flow, including fixed points and a discussion of phase plots and the frequency spectrum of several key points in the flow. The behavior of invariant manifolds directly relates to the flow topology and illuminates some aspects seen in phase space during vortex shedding. Furthermore, it highlights the reattachment behavior in ways not seen before.

PACS numbers: 47.10.−g, 47.11.−j, 47.32.−y, 45.20.Jj

(Some figures in this article are in colour only in the electronic version)

1. Introduction

1.1. Background

Micro aerial vehicles (MAVs) have recently become a topic of significant effort in scientific communities. The unique challenges and opportunities that MAV technology offers have resulted in increased interest in topics such as flexible wing, flapping wing and low Reynolds number aerodynamics. This paper specifically targets the behavior of low Reynolds number reattachment and vortex shedding for potential MAV applications. There exists a multitude of

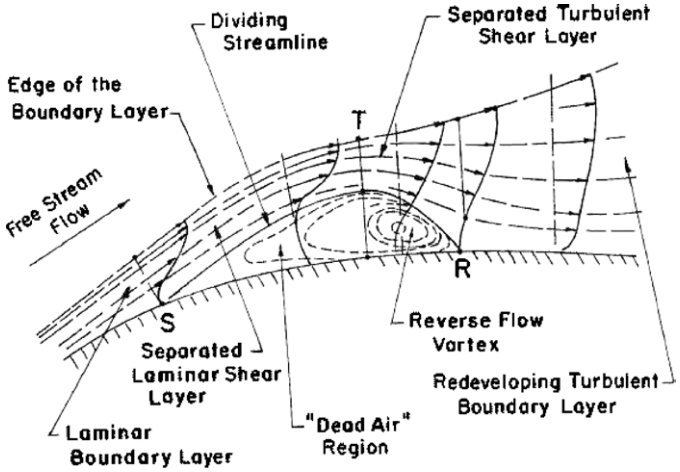

Figure 1. Classical diagram of separation bubble structure [1].

previous work regarding the behavior and properties of separation and vortex shedding. Early work in the field of separation was highlighted by Hornton in 1968 [1] who introduced the now well-known time averaged laminar separation bubble model. Continuing work focused on behavior behind a backward facing step [2, 3], pressure-induced separation [4] and separation behind airfoils [5–7]. These studies utilized velocity fields (both numerical and experimental), vorticity contours and streamlines to observe the behavior of vortex shedding. The result of this work is a detailed understanding of the separation profile, vortex pairing and vortex shedding, and their effect on airfoil performance. The discussion regarding reattachment behavior, on the other hand, has previously been limited to time-averaged results. Thus several issues remain to be investigated, including the time-dependent behavior of reattachment, the detailed structure of fluid mixing and how the shed vortices form. Understanding this behavior may lead to advances in flow actuation theory by highlighting key structures and times in the flow including structures below and in front of the airfoil. Although the behavior of unstable manifolds over an airfoil without vortex shedding has recently been investigated [8], this investigation will examine the behavior of both stable and unstable manifolds associated with reattachment and vortex shedding behind an airfoil.

Although the separation profile is well understood, little is known about the time-dependent reattachment profile. Reattachment is equally important since the size of the separation bubble is largely determined by the reattachment point. Manipulation of the separation bubble is critically important to the aerodynamic performance of a vehicle. This is achieved through various methods aimed at manipulating the separation or reattachment points. One of the goals of the present study is to provide insight into how the reattachment profile behaves by utilizing invariant material manifolds. By exploring the formation of shed vortices, this study will aim to elucidate critical moments and locations in the formation process which may be particularly useful for manipulation.

1.2. Material manifolds

The steady laminar separation bubble is defined by the dividing streamline shown in figure 1 [5]. In a time-averaged view, the material flux across the profile is zero. For our setup, low *Re*

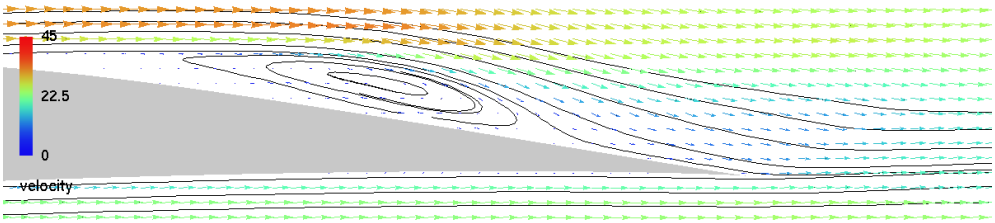

Figure 2. Time-averaged velocity and streamlines for low Reynolds number flow. $\alpha = 4^\circ$, $Re = 60\,000$, Eppler 387 airfoil [10].

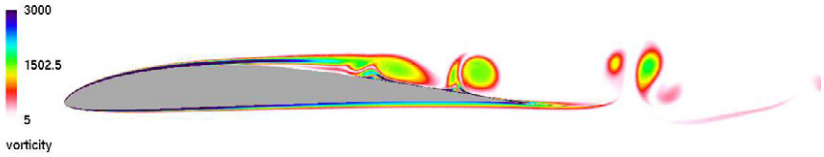

Figure 3. Representative vorticity map for low Reynolds number flow. $\alpha = 4^\circ$, $Re = 60\,000$, Eppler 387 airfoil [10].

flow over an airfoil at $\alpha = 4^\circ$, the time-averaged velocity field and streamlines are shown in figure 2. Investigating how this bubble behaves in real time on the other hand has proven difficult, in part due to the complications involved in identifying the reattachment lines. Traditional flow maps such as the vorticity (figure 3) can be used, but vorticity contours do not have the inherent zero mass flux property that we desire. Instantaneous streamlines are somewhat better, but show little detail in flow structures. Invariant material manifolds, on the other hand, delineate clear transport barriers and separate the flow into distinct regions [9]. These manifolds may be either repelling or attracting material manifolds, but in either case, the flux across the manifolds is negligible, and this is the property we require to visualize the separation bubble in real time.

The repelling material lines, also known as stable manifolds are responsible for the stretching of passive tracer groups normal to the manifold while attracting material lines, also known as unstable manifolds are responsible for the stretching of tracer groups tangent to the manifold [11]. When an unstable manifold is attached to a wall, fluid particles are drawn from the near wall region and ejected along the manifold path. Thus the separation profile of the flow should correspond with an unstable manifold. The reverse is true for stable manifolds attaching to a wall; their profile represents the reattachment line. For the remainder of this manuscript we will provide a brief overview of Lagrangian coherent structures as material manifolds and observe the behavior of the invariant manifolds. We will also demonstrate the relationship between particle motion and the manifold profiles. We will also explore the behavior of fixed points and flow topology. Finally, we will examine the phase plane behavior of several points in the flow. We find excellent agreement between all these methods of analysis and conclude with a detailed understanding of the flow structure and behavior during vortex shedding.

2. Lagrangian coherent structures

2.1. LCS and invariant manifolds

Lagrangian coherent structures (LCS) were first introduced by Haller *et al* [12] in 2000. Haller defines LCS as material lines with locally the longest or shortest stability or instability time. In dynamical systems theory, such structures are referred to as stable and unstable manifolds and will hereafter be referred to as such. Our research objective is to locate and analyze these manifolds, and for that analysis LCS theory is a useful tool. In practical applications, LCS are defined as ridges of the finite time Lyapunov exponent (FTLE) field [8]. These ridges represent the material lines or manifolds in the flow which are characterized by very low flux across the profile. The manifolds are unique and time dependent and due to their invariance their interaction with one another is largely responsible for fluid mixing.

2.2. Calculation of LCS

For our calculation of FTLE fields, we will closely follow the procedure set forth by Shadden *et al* [8]. It should be noted that FTLE fields are not the only method for identifying LCS [13], FTLE was chosen for this study because it is well suited to a discrete velocity field defined on a finite time interval. Following Shadden *et al* [8], once a velocity field has been defined (numerically, experimentally or analytically), the region to be analyzed is seeded with a dense mesh of passive fluid tracers. The tracers are advected with the flow for an integration time τ and the Cauchy–Green deformation tensor, Δ, is calculated for each point based on the deformation of the tracer mesh. The FTLE is then defined in terms of the maximal stretching based on Δ as

$$\sigma_{t_0}^{\tau}(x) = \frac{1}{|\tau|} \ln \sqrt{\lambda_{\max}(\Delta)}, \tag{1}$$

where $\lambda_{\max}(\Delta)$ is the maximal eigenvalue of Δ. Stable and unstable manifolds are then defined as ridges in the FTLE field with $\tau > 0$ for stable manifolds and $\tau < 0$ for unstable manifolds. For this study, the velocity field was given by the results of a computational fluid dynamics (CFD) simulation for the flow around the airfoil. For details of the numerical procedure for the CFD simulation see [14]. The FTLE field was calculated using a code developed for this purpose.

3. Procedures

In this simulation, two-dimensional flow over an Eppler 387 airfoil is examined. The free stream velocity is 30.89 m s^{-1} and the Reynolds number is $Re = 60\,000$. This wing type has been previously used for MAVs [15] and $Re = 60\,000$ is in the typical range of MAV operation [16]. The run was performed in a non-dimensional mode, defining the free stream velocity as 1 unit length/unit time. A unit length is defined as the chord length, and a unit time therefore is the chord length divided by the freestream velocity. The results showed a vortex formation shedding frequency of approximately 2.4 shedding cycles per unit time. A time step of $t = 0.0015$ unit time is used for accuracy, but to conserve memory only every 8th timestep is stored. Therefore, the time step for the exported data files is $t = 0.012$ time units. The partitioned, unstructured velocity field files are then compiled by our FTLE program, creating node and element connection lists, and initializing search protocols. The desired area for calculation of FTLE values is specified by the user's designation of the drifter mesh. The software uses an alternating digital tree algorithm [17] to search the domain for

the element containing each indexed drifter, the velocity is interpolated onto this point using shape functions, and the location and velocity information are stored for future steps. The indexed drifters are advected forward in time using a 4th order Runge–Kutta scheme. In this simulation, 240 velocity time steps were analyzed, for $\alpha = 2^\circ, 4^\circ$ and 6°. The Cartesian mesh of drifters covered the domain $-1 \leqslant x \leqslant 1.5, -0.5 \leqslant y \leqslant 0.5$, with a uniform grid spacing of $\Delta x = \Delta y = 0.0012$ units. This grid spacing was necessary to capture the fine detailed structures in the wake region and to ensure the accuracy of the manifold calculations. The accurate calculation of LCS structures requires that the grid spacing be small [11]. The integration time was set to $|\tau| = 0.72$ time units to optimize the appearance of the desired flow structures. Longer integration times reveal more detail, but the important structures become obscured by unimportant features while shorter integration times fail to reveal the desired level of detail.

4. Behavior of manifolds

4.1. Unstable manifolds

Contour plots of the backward time ($\tau = -0.72$) FTLE field showing unstable manifold structures are shown in figure 4 for a full shedding cycle. Major recurring coherent structures in the flow are marked by U1–U7 in this figure. These manifolds are represented by well-defined ridges in the FTLE contour plot, shown as dark lines (online version: red and orange lines). Figures 5, 6, 7 and 8 show magnified views of the most interesting regions. In figure 4, the farthest upstream unstable manifold (labeled U1) which attaches to the airfoil is the separation point in the flow. This manifold is well defined and is observed to be largely time invariant.

Although the separation point has been studied extensively in the past, it remains the source of some confusion in the case of unsteady flows. Haller has shown that for incompressible flow, the effective separation point is just the point of zero mean skin friction on the airfoil [18]. In the case that the point of zero skin friction is time invariant, the separation point is also time invariant. In previous analysis of this flow, this point has been observed to be time invariant (see figure 3.6 of [10]) and the separation point is therefore stationary. Underneath this manifold is a region of stalled flow, known as the separated shear layer, which will be examined in more detail shortly. Moving downstream we note four prominent manifolds as shown in figure 6. The manifolds U2 and U3 (figure 6(*a*)) coincide with forming vortices and have a well-defined structure which forms an attachment between the vortices. Another manifold, U4 (figure 6(*c*)), on the airfoil surface is very strong and will eventually become a part of the shed vortex. This manifold is associated with the secondary induced vortex. Finally, the manifold immediately upstream of U4 will be shown to be responsible for transporting many fluid particles upstream into the stalled flow region. Note, as time progresses, that several of these coherent structures collide and connect in several places, and as vortices are shed from the trailing edge new manifolds evolve upstream to form the next set of vortices.

Downstream of the trailing edge, there are two distinct FTLE ridges which should be noted. The most prominent structure is the connection between the counter-rotating shed vortices (U7) as seen in figure 4(*a*). This manifold is one of the strongest to appear anywhere in the flow field, and shows that there exists a well-defined separation between the two shed vortices and the surrounding flow that is not clear in plots of vorticity or streamlines. In fact, U2 (figure 4(*a*)) is the same manifold as U7, but for the next pair of vortices which have yet to be shed. The second is another strong manifold attached to the trailing edge of the airfoil (U6, figures 4(*a*) and 8(*a*)). As a vortex is shed, this manifold is stretched and wrapped into

Figure 4. Contour plots of FTLE over airfoil, U1–U7 are the major recurring structures in the flow, online version shows these ridges in red and orange.

Figure 5. LCS profile at separation point.

the core of the vortex. This deformation of U6 occurs near the trailing edge, but does not destroy the structure of U6. Instead, the remnants of the manifold become attached to the

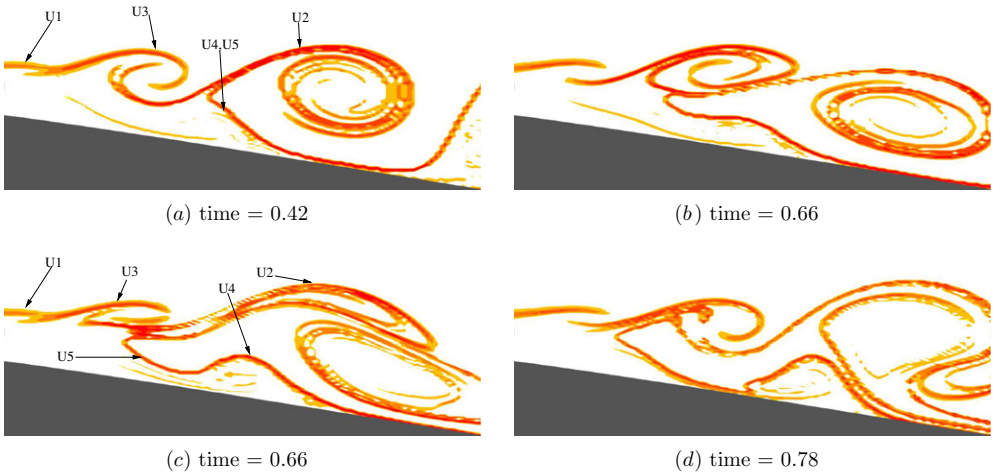

(a) time $= 0.42$ (b) time $= 0.66$

(c) time $= 0.66$ (d) time $= 0.78$

Figure 6. Unstable manifold behavior along upper surface of airfoil during vortex shedding.

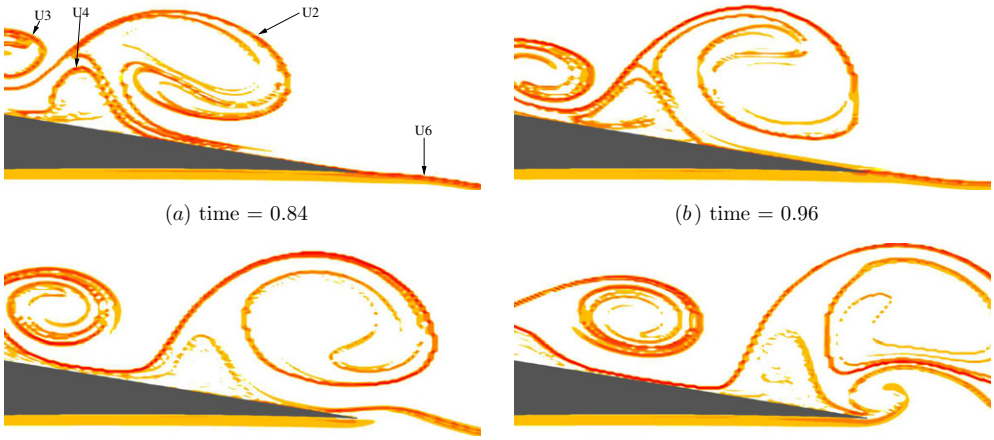

(a) time $= 0.84$ (b) time $= 0.96$

(c) time $= 1.08$ (d) time $= 1.20$

Figure 7. Unstable manifold behavior at the trailing edge of an airfoil during vortex shedding.

leading shed vortex and a new connection is established. This behavior is in actually part of a surprising process which corresponds with fluid entrainment from below the airfoil into the shed vortices. As the second vortex in the shed pair leaves the trailing edge we can see a single coherent structure linking the trailing edge of the airfoil to the past two shed vortex pairs. The connection between shed vortices begins to weaken as they move farther downstream.

Introducing fluid tracers to the flow field allows us to examine the interactions between the unstable manifolds and particle motion. Drifters are initially located at $x = 0$ and for each grouping, 91 drifters are released and advected forward in time. In figure 9, drifters have been released at times 0.24 time units apart; each new set of particles is represented by a new symbol and color.

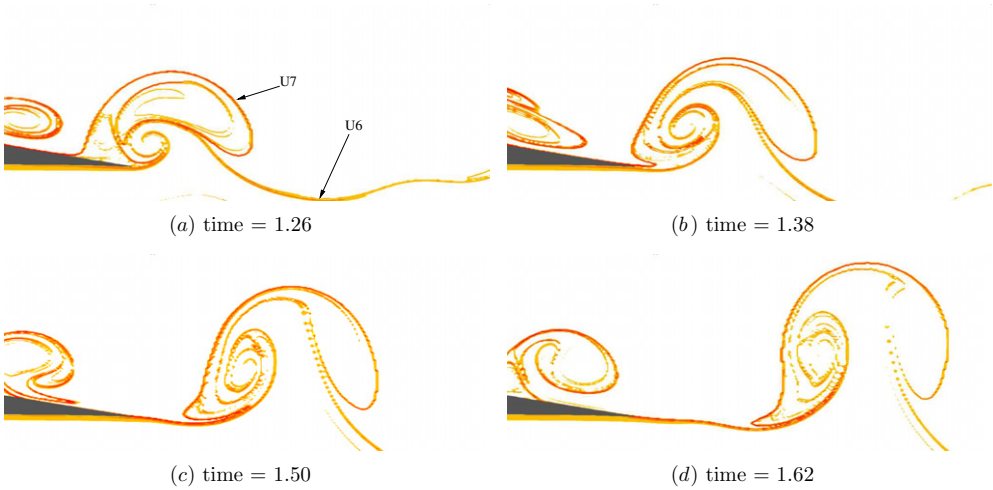

(a) time $= 1.26$ (b) time $= 1.38$

(c) time $= 1.50$ (d) time $= 1.62$

Figure 8. Unstable manifold behavior past the trailing edge of an airfoil during vortex shedding.

As expected, most of the drifters eventually find their way onto or very near one of the unstable manifolds in the flow. This is independent of when the drifters are released; the release frequency was chosen to enhance clarity. Instead, this is due to the fact that unstable manifolds are attracting material lines. Attracting material lines are responsible for localized thinning and folding of the flow as well as stretching in the direction tangent to the manifold [12]. In fact, Haller and Yuan [12] show in their paper that a group of densely packed passive tracers involved in mixing can show the locations of attracting material lines by simply watching how the particles begin grouping and stretching to form regions and lines of very dense and very sparse concentrations of particles. This behavior in the airfoil wake region provides evidence that the unstable manifolds identified really behave as attracting material lines. Further evidence may be found in figure 10 in which we see the time progression of a grouping of particles approaching manifold U2.

The particles in figure 10 are pushed up by the secondary induced vortex (manifold U4) on the surface of the airfoil and impact approximately normal to the line U2 at point A1 in figure 10(c). This group of fluid tracers is split apart by the manifold, some to be entrained into the vortex core, others to continue moving upstream.

Those particles which are not captured by the vortex move upstream toward the stalled flow region as shown in figure 11. Note that while traveling upstream a great percentage of these drifters are concentrated near manifold lines. Additionally, it is observed that those particles closest to the manifolds appear to move upstream more quickly than those not near a manifold. This behavior is expected per Inanc *et al* [19]. The fluid particles which continue moving upstream into the stalled flow region are transported there along manifold U5. This manifold repeatedly regenerates, moves upstream and dissolves in the stalled flow region, leaving the particles there. The correlation between manifold behavior and particle behavior offers opportunities for flow manipulation. Since the manifolds dictate where particles may go, it is enough to manipulate the manifold's shape to change the flow structure. If the location of an unstable manifold could be established in real time, small manipulations of the manifold at the airfoil surface may have significant effects on particles along the manifold profile, but far away from the airfoil surface.

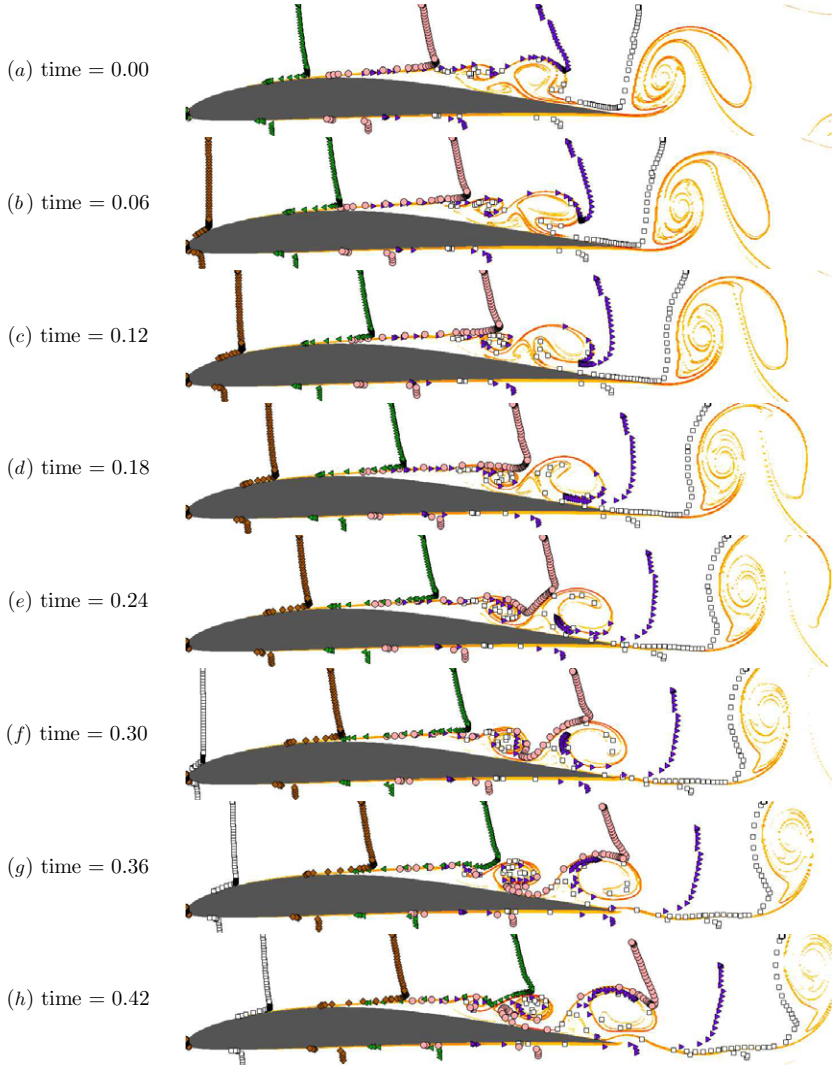

Figure 9. FTLE contour plot with passive fluid tracers overlaid. Five groups of 91 drifters released with frequency 0.833 beginning at $t = -0.948$. Group 1: □ (online: white), group 2: ▶ (online: purple), group 3: ○ (online: pink), group 4: ◀ (online: green), group 5: ♦ (online: brown).

4.2. Angle of attack and vortex pairing

So far we have focused on behavior over an airfoil with 4° angle of attack. Unsurprisingly, the angle of attack has a noticeable impact on manifold behavior. For this study we have examined the behavior at 2°, 4° and 6° angles of attack. Figure 12 shows the comparison of these three angles of attack for a typical point in their vortex shedding cycle. Note that the structures share common traits in all three cases. As expected, the separated region begins farther upstream as α is increased. A closer inspection of the manifolds shows another trend. The secondary induced vortex, which we will shortly label as V5, appears to be more energetic as the angle of attack increases. For our purposes it was determined that the six degree angle of attack

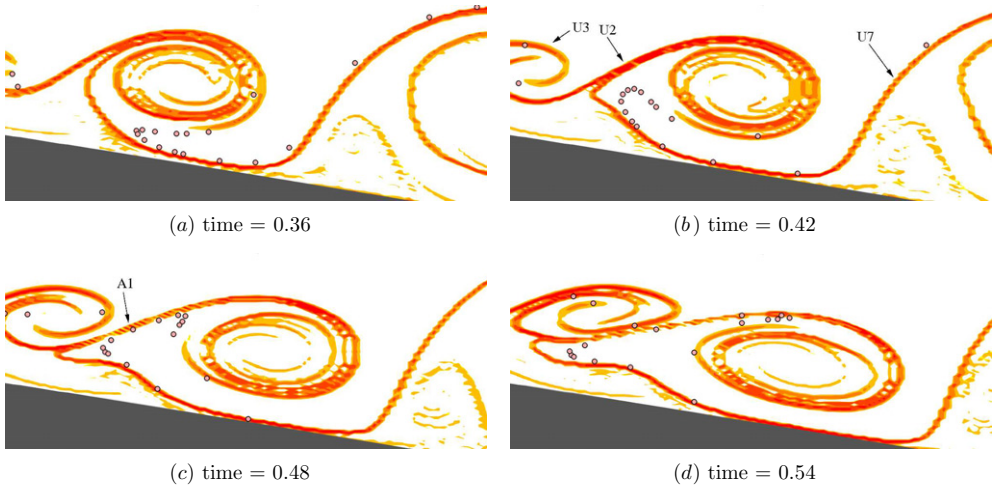

(a) time = 0.36 (b) time = 0.42

(c) time = 0.48 (d) time = 0.54

Figure 10. Drifters from group 3 incident upon LCS line U2.

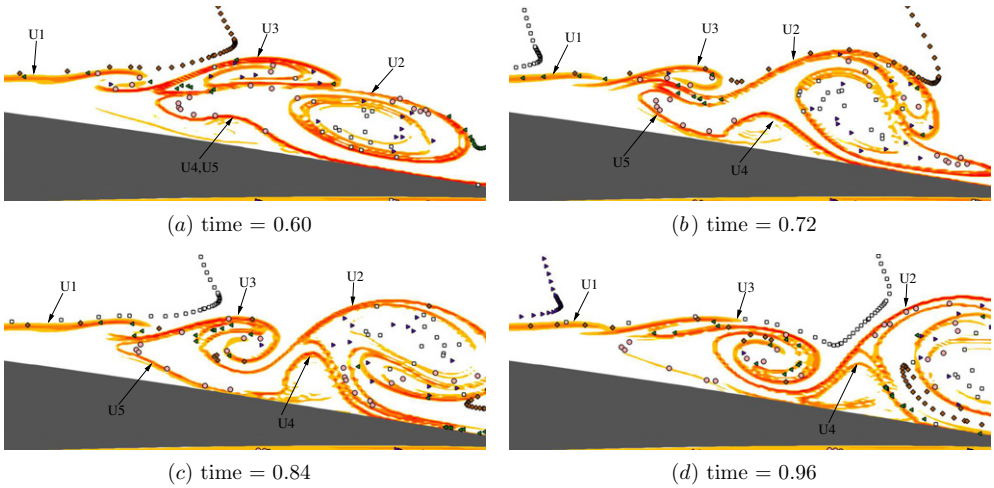

(a) time = 0.60 (b) time = 0.72

(c) time = 0.84 (d) time = 0.96

Figure 11. Drifters from all groups demonstrating the effect of LCS U4 and U5 on transporting drifters upstream in the stalled flow region.

presents the most illustrative cases for vortex pairing. Thus, for the following sections the focus of our study will shift to $\alpha = 6^\circ$.

Figure 13 shows the time evolution of the unstable manifolds at $\alpha = 6^\circ$. The similarities to $\alpha = 4^\circ$ case are numerous, but here we will focus on the behavior of individual vortices. Using traditional flow maps (e.g. vorticity), the individual vortices become indistinguishable from each other once they are paired. Using material manifolds, we can track the remnants of the individual vortices for a much longer time. Figure 13 shows the unstable manifold representation of vortex pairing. Beginning in figure 13(a), we track the formation and movement of four distinct regions (V1–V4) that eventually form the large scale vortex shed from the trailing edge. Even though there is extensive deformation of the individual structures

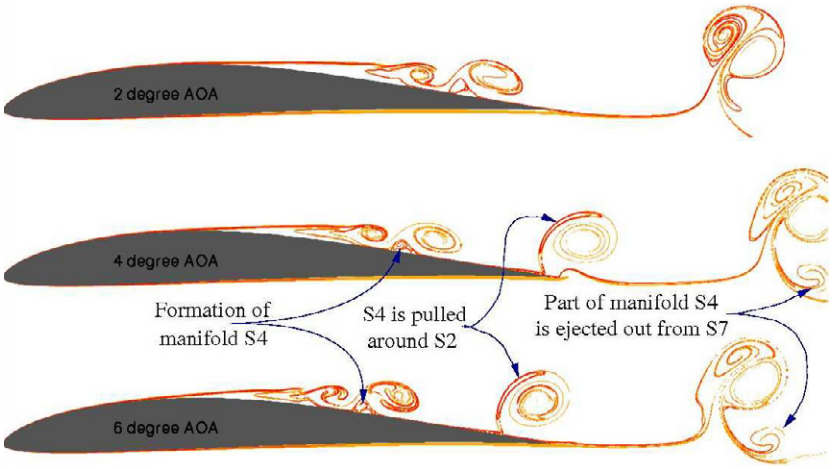

Figure 12. Comparison of the LCS manifolds at different angles of attack.

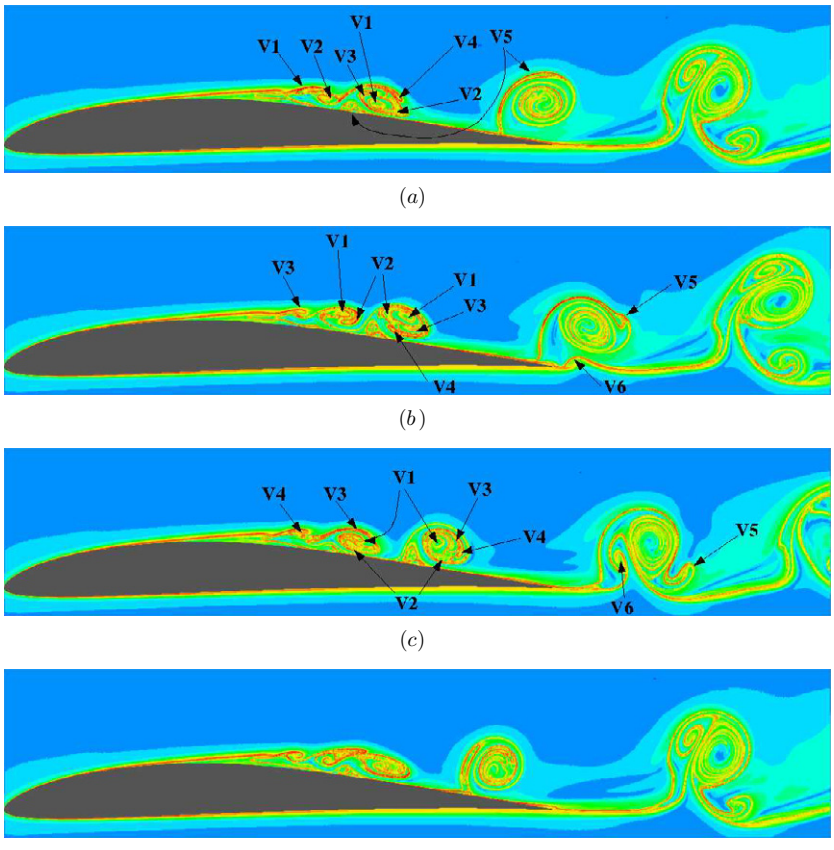

Figure 13. Contour plots of backward time FTLE over airfoil representing the unstable manifolds, $\alpha = 6^{\circ}$, $Re = 60\,000$.

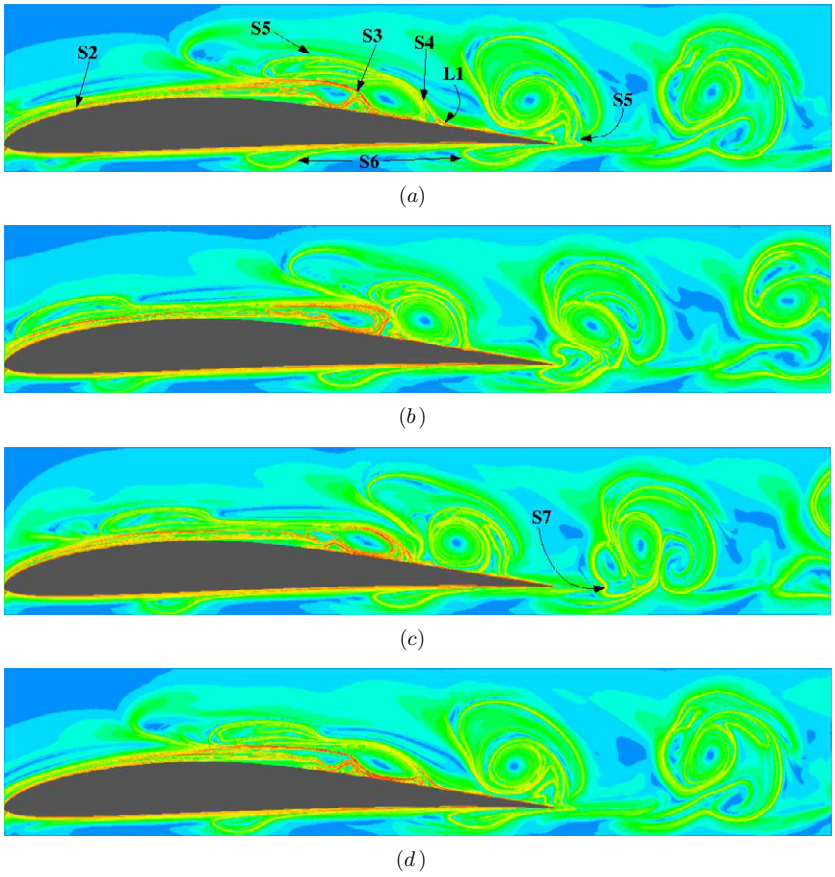

Figure 14. Contour plots of forward time FTLE over airfoil representing the stable manifolds, $\alpha = 6^\circ$, $Re = 60\,000$.

throughout formation, by using material manifolds we can track the remnants of each until it nears the trailing edge at which point the manifolds begin to lose their definition as seen in figure 13(*d*). As the vortex leaves the trailing edge, two additional regions are picked up, V5 and V6, figure 13(*b*). Vortex V5 is the secondary induced vortex from the airfoil surface, and V6 is the counter rotating tip vortex which contains material from below the airfoil's surface. V6 gets paired with the shed vortex and they move downstream as a pair. Vortex V5 is picked up from the top surface as the vortices approach the trailing edge, and gets rolled around the top boundary of the vortex pair to finally settle downstream of the main vortices as shown in figure 13(*c*). The rest of the behavior for the unstable manifolds at six degree angle of attack is consistent with the behavior examined previously at $\alpha = 4^\circ$.

4.3. Stable manifolds

Our discussion of unstable manifolds was initially motivated by the presence of an unstable manifold which delineates the separation profile. To further our understanding of the separation bubble, we now shift to an analysis of stable manifolds for a 6° airfoil under the same conditions, which we expect to reveal the reattachment profile. Figure 14 shows the time evolution of the

stable manifolds over the airfoil. Note that while we can identify the large scale structures, most of the manifolds in this view do not look like the familiar vortices we may expect. This is because calculating the stable manifolds involves using our future knowledge of how the flow field will behave. If we focus on the reattachment behavior we see that there is a clear reattachment point found at location L1 in figure 14(*a*). The manifold attached to this point, S4, is clearly a ridge in the FTLE field, but it is not as strong of a ridge as we might expect the reattachment profile to display. In fact, it is clearly not the dominant feature in figure 14(*a*). This is due to the shedding behavior of the flow which leads to a periodic dissolving and reforming of the reattachment manifold.

In figures 14(*b*) and (*c*), manifold S4 weakens, but S3 transforms into a new shape, forming a new reattachment manifold which is visible in figure 14(*c*), but has an unexpected shape. By figure 14(*d*), the expected reattachment profile as seen in time-averaged separation bubbles has reappeared. Manifold S4 weakens just as vortex V4 (figure 13) joins the paired vortices as seen in section 4.1. This signifies the completion of the vortex pairing at which point the newly formed vortex begins moving downstream.

There are two additional structures that are very interesting. Manifolds S5 and S6 appear as weak, but distinct ridges above and below the airfoil in figure 14(*a*). Figure 14(*b*) shows that manifold S5 has been pulled around the shedding vortex and eventually manifolds S5 and S6 leave the trailing edge together, merging to create manifold S7. The appearance of manifold S7 coincides with the formation of the roll up vortex seen in section 4.1. The fluid particles contained inside manifolds S5 and S6 are the same fluid particles which will eventually make up the rolled up vortex. This reveals unexpected structure to the flow underneath the airfoil. From a flow control perspective, it suggests that utilizing flow control on the lower surface and targeting this manifold could cause changes in the vortex shedding structure. Also, it shows that the flow which eventually forms the roll-up vortex exists as two distinct and intact groups well ahead of the point where the roll up occurs. In fact, manifold S5 first appears upstream of the leading edge, while manifold S6 forms just downstream of the stagnation point. These observations have been further examined by Cardwell and Mohseni [20].

4.4. Stable and unstable paired manifolds

Together the stable and unstable manifolds are known to define regions or lobes of distinct particle mixing [9]. Thus, for a complete understanding of the flow topology we need to combine the two to learn how they interact. Combining the stable and unstable manifolds will reveal exact vortex boundaries (as demonstrated in [21]), locations where entrainment is possible, and the time-dependent profile of the separation bubble. Figure 15 shows the limited time evolution of the two manifolds. In this case, we have plotted the more familiar structure of the unstable manifolds as a contour map of the FTLE values, and then overlaid a clipped contour map of the stable manifolds and colored these black. The result is a complete map of the manifolds involved in vortex shedding. As expected, the manifolds often meet and sometimes overlap. This demonstrates that flow boundaries are a combination of stable and unstable manifolds just as Shadden *et al* [21] have shown for a vortex ring. Note that the shed vortex in figure 15(*a*), largely defined by the unstable manifolds, is closed by the stable manifold.

The most interesting and complicated behavior occurs inside the separation bubble. This behavior is more clearly shown in figure 16 where the domain has been restricted. In this figure, the impact of manifold S3 is revealed. Beginning during vortex formation, the S3 manifold isolates the formation region from all flow but the inlet, where the new vortices will draw their strength from. S3 also separates the just forming vortices from the vortices which

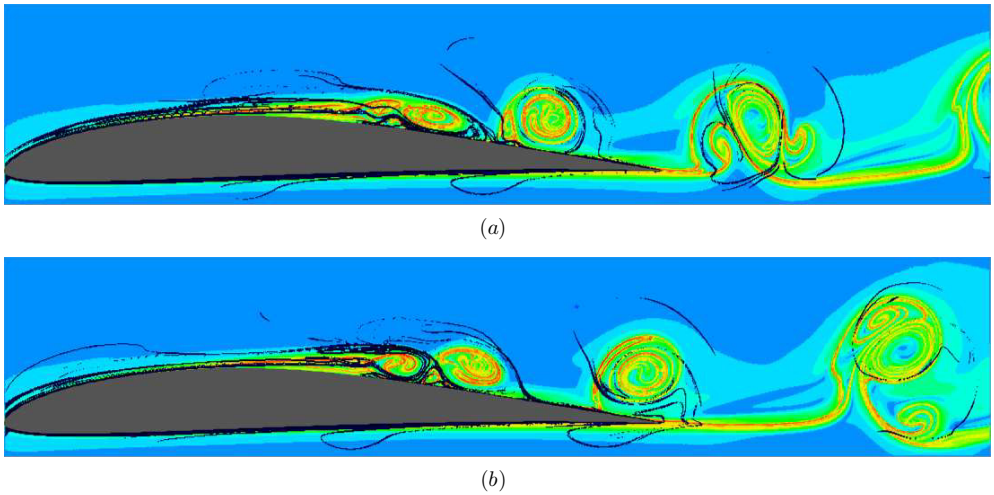

Figure 15. Contour plots of forward and backward FTLE over airfoil representing the stable (black) and unstable (colored) manifolds, $\alpha = 6^\circ$, $Re = 60\,000$.

are peeling off from the separation bubble to move downstream. As time evolves, manifolds S2 and S3 take on more definition as S4 is eroding. Soon S3 has begun to lose some of its defining shape, while the S2 manifold begins to acquire these same shapes. This is the evolution of manifolds in action. S2, S3 and S4 are really the same periodically forming manifolds which separate pairs of vortices from one another. Although we can affix labels to the manifolds at a given instant of time, they will continuously evolve and soon no longer contain any of their initially defining features.

Perhaps one of the most interesting insights that the pairing of stable and unstable manifolds gives us is a defined boundary for the separation bubble which we can watch evolve and change during a shedding cycle. Though it may be difficult to interpret in some places due to its dynamic nature, the region near the airfoil bounded by the stable and unstable LCS manifolds is the separation bubble. The fact that this bubble may have openings in it is expected since the traditional definition of a separation bubble as having zero mass flux is based on a time-averaged view. In this case we are watching the separated region deform in real time. Since there is zero flux across the manifolds shown flow into and out of the separation bubble must come through the gaps in these manifolds during the shedding process.

5. Flow topology

To gain additional information about the vortex shedding and reattachment, we now focus on a topological overview of the flow as determined by analyzing streamlines in the flow. See figure 17 for an overview of three representative times in the development of the flow topology. First, we verify the viability of these topologies by checking that the fixed points satisfy the relationship developed by Hunt *et al* [22] for the relative number of fixed points in the flow:

$$\left(\sum E + \frac{1}{2}\sum E'\right) - \left(\sum H + \frac{1}{2}\sum H'\right) = 1 - n, \tag{2}$$

where E and H represent four-way elliptic and hyperbolic fixed points, E' and H' represent three-way elliptic and hyperbolic fixed points and n is the connectivity of the region, in our

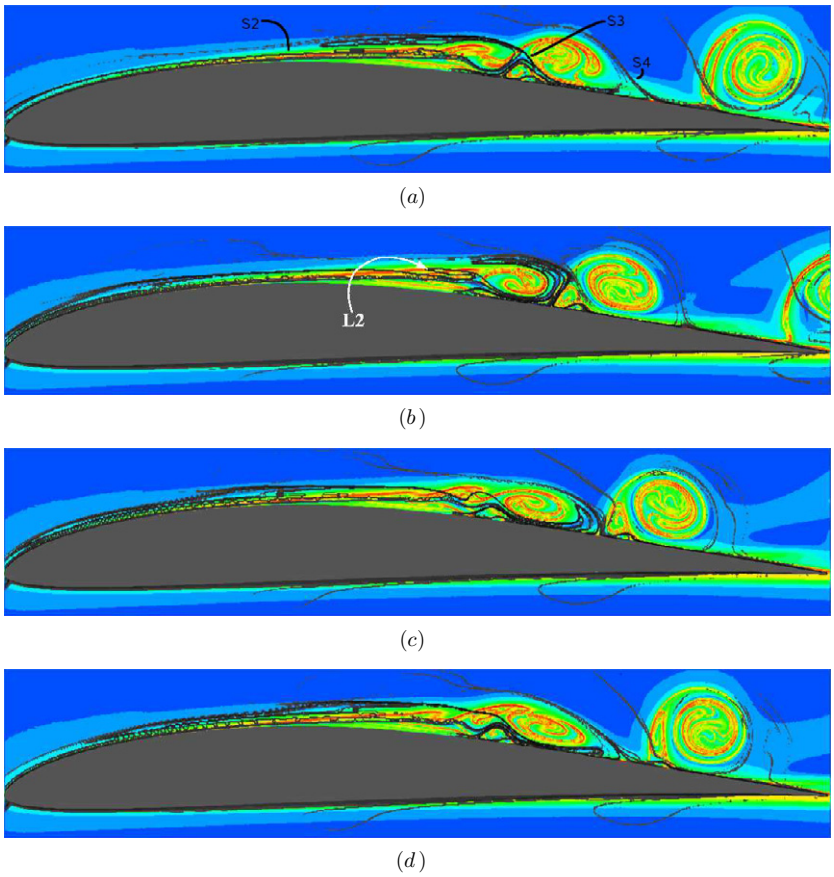

(*a*)

(*b*)

(*c*)

(*d*)

Figure 16. Contour plots of forward and backward FTLE over airfoil representing the stable (black) and unstable (gray or colored online) manifolds, $\alpha = 6^\circ$, $Re = 60,000$.

case $n = 2$. All three topologies satisfy this relationship with figure 17(*a*) and (*b*) having $E = 6$, $E' = 0$, $H = 2$ and $H' = 10$. The topology in figure 17(*c*) adds an extra elliptic and hyperbolic fixed point.

It is interesting to follow the development of fixed points in the flow. Figure 17(*a*) shows a separation bubble with a vortex moving toward the trailing edge of the airfoil. As figure 17(*a*) transitions to 17(*b*), H1 and E1 move toward the rear of the separation bubble and the vortex centered on point E2 is ready to be shed. As figure 17(*b*) transitions to 17(*c*), a reverse saddle-node bifurcation occurs as points H1 and E1 collide, destroying each other and separating a new vortex from the separation bubble. At the same time, the three way hyperbolic points, H2 and H3 collide and separate from the airfoil's surface, creating a new four-way hyperbolic point just below the shed vortex. The collision of H2 and H3 and subsequent separation from the airfoil represents a fundamental change in the topology of the flow as a vortex is shed. Finally, a new elliptic fixed point forms near the airfoil's surface in the upstream portion of the separation bubble. This fixed point forms as the flow here pulls away from the airfoil's surface and also creates two new three-way hyperbolic fixed points. After all of this, figure 17(*c*) transitions back to 17(*a*) as the fixed points in the shed vortex merge, canceling

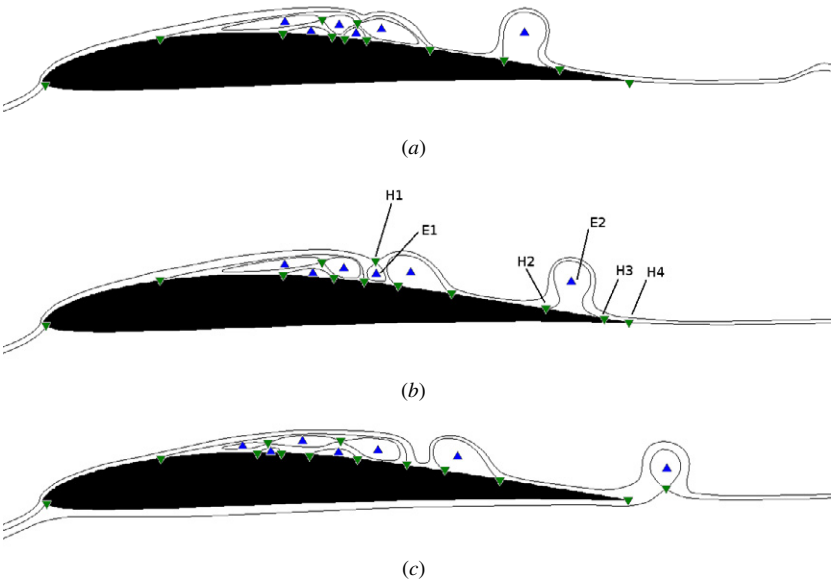

(*a*)

(*b*)

(*c*)

Figure 17. Flow topology of vortex shedding at three representative times. ▲ designate elliptic fixed points, ▼ designate hyperbolic fixed points.

Figure 18. Fixed points in the flow, overlaid on top of stable and unstable manifolds. Online version shows unstable manifolds in red, stable manifolds are overlaid in gray. Hyperbolic fixed points are gray squares (green online) (■), elliptic fixed points are black squares (dark blue online) (■).

each other in another reverse saddle-node bifurcation and the newly formed vortex which has just split from the separation bubble begins moving down the airfoil.

These processes closely match what we previously observed in the invariant manifolds. The saddle-node bifurcation involving H1 and E1 corresponds with the manifold previously labeled U4 in section 4.1 beginning to push upward, separating the developing vortex from the separation bubble. At the same time, the reattachment profile is reforming upstream. The new reattachment profile lies along manifold S3 as seen in figure 14(*a*) which is seen in figure 17(*c*) as the back of the separation bubble.

Fixed points in the flow also closely relate to the coherent structures we have seen previously. Figure 18 shows the position of fixed points in the flow overlaid with the stable and unstable manifolds. Note that the hyperbolic fixed points largely correspond with intersections between the stable and unstable manifolds and the elliptic fixed points occur inside vortices

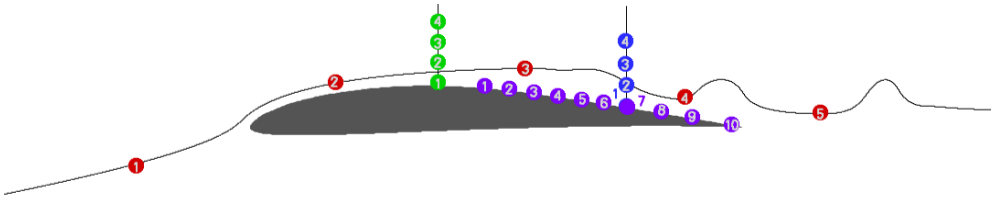

Figure 19. Locations where phase portraits were calculated. Points R1–R5 (red online) lie on a streamline above the airfoil, points G1–G4 (green online) lie along the upstream vertical line near the separation point, points P1–P10 (purple online) lie just above the airfoil's surface in the vortex formation region and points B1–B4 (blue online) lie in the downstream vertical line in the vortex formation region.

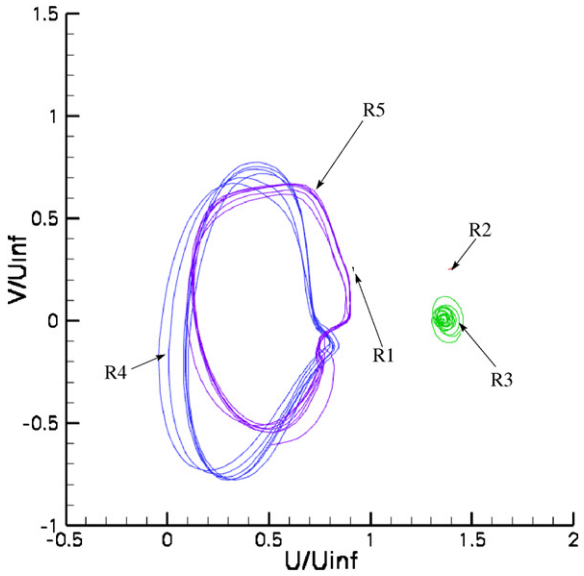

Figure 20. Phase portrait of red points along streamline shown in figure 19.

identified by these manifolds. This correspondence is indicative of the fact that invariant manifolds convey information similar to the flow topology, but with the additional property of zero flux through the manifolds.

6. Phase plots

There are two main ways of looking at any dynamical system, in physical space or phase space. Up to this point, we have focused on the physical space of our system, so to finalize our analysis of the vortex shedding process we now turn to a discussion of phase portraits and the dominant frequencies at several representative points in the flow. Figure 19 shows the locations of 24 points where the velocity variations were tracked. Points R1–R5 (red online) lie on a streamline above the airfoil, points G1–G4 (green online) lie along the upstream vertical line near the separation point, points P1–P10 (purple online) lie about 0.001 chord lengths above the airfoil's surface in the vortex formation region and points B1–B4 (blue online) lie in the downstream vertical line in the vortex formation region. Each set of points has been numbered

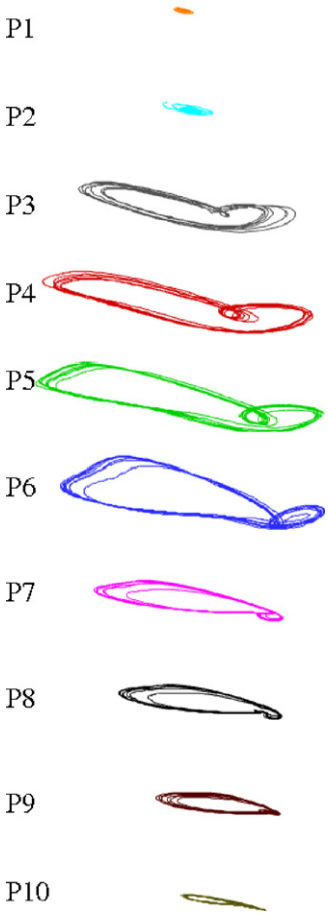

Figure 21. Phase plots of the purple points located along the surface of the airfoil where vortex formation occurs, as shown in figure 19. The x-axis is u-velocity and the y-axis is v-velocity.

and plotted in figures 20–23. The varying amplitude seen in the phase plot corresponding to the streamline points in figure 20 shows how the energy increases as the flow passes over the airfoil and then begins to decrease downstream. Points R1 and R2 show very little velocity disturbance upstream of the separation point. Moving past the separation point we see the disturbances begin to build at point R3, but are somewhat chaotic. Points R4 and R5 lie in the region where vortices are well formed and because of this exhibit highly periodic behavior. An analysis of the frequency spectrums reveals a dominant frequency corresponding to the vortex shedding frequency and a strong secondary frequency at twice this rate (see figure 24). In fact, all points downstream of P3 except B4 show the same two dominant frequencies in their spectrum (more on this later). The secondary frequency appears because the main vortex is formed by two initially distinct vortices which pair with one another. This results in the observed frequency doubling.

If we turn our attention to the points along the airfoil surface, figure 21 shows how the variations grow and have well-defined periodic structures. This is of particular interest because these points are located near the surface of the airfoil and if the velocity can be measured in real time, it would be possible to determine precisely where in the vortex shedding process the flow is, providing feedback for flow actuation methods. Points P1 and P2, although in

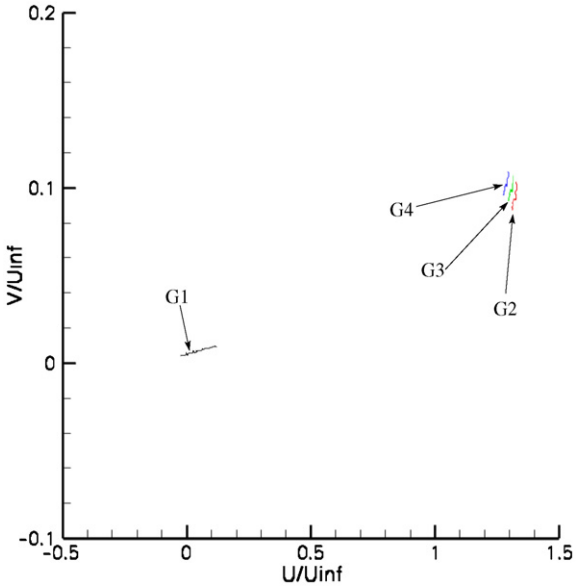

Figure 22. Phase portrait of green points along upstream vertical cross-section of flow shown in figure 19.

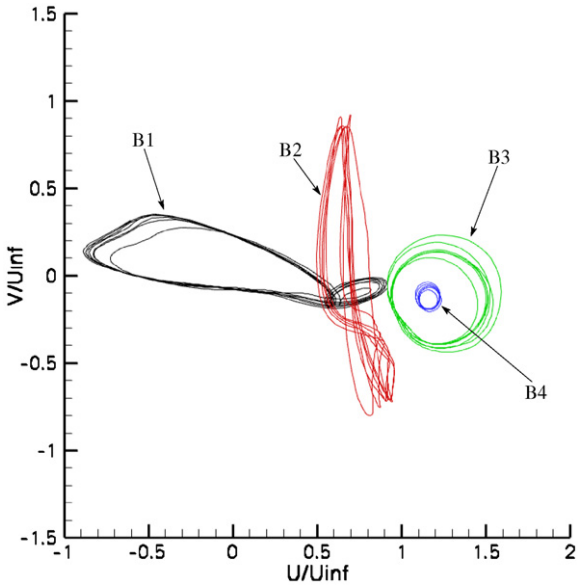

Figure 23. Phase portrait of blue points along downstream vertical cross-section of flow shown in figure 19.

the separation bubble, lack the secondary frequency seen in the downstream points due to their location in the dead air region upstream of the first elliptic fixed point seen in figure 17. As expected, the G1–G4 (green online) points, figure 22, show very little fluctuation in the flow since they are located near the separation point. Contrastingly, if we look at the B1–B4

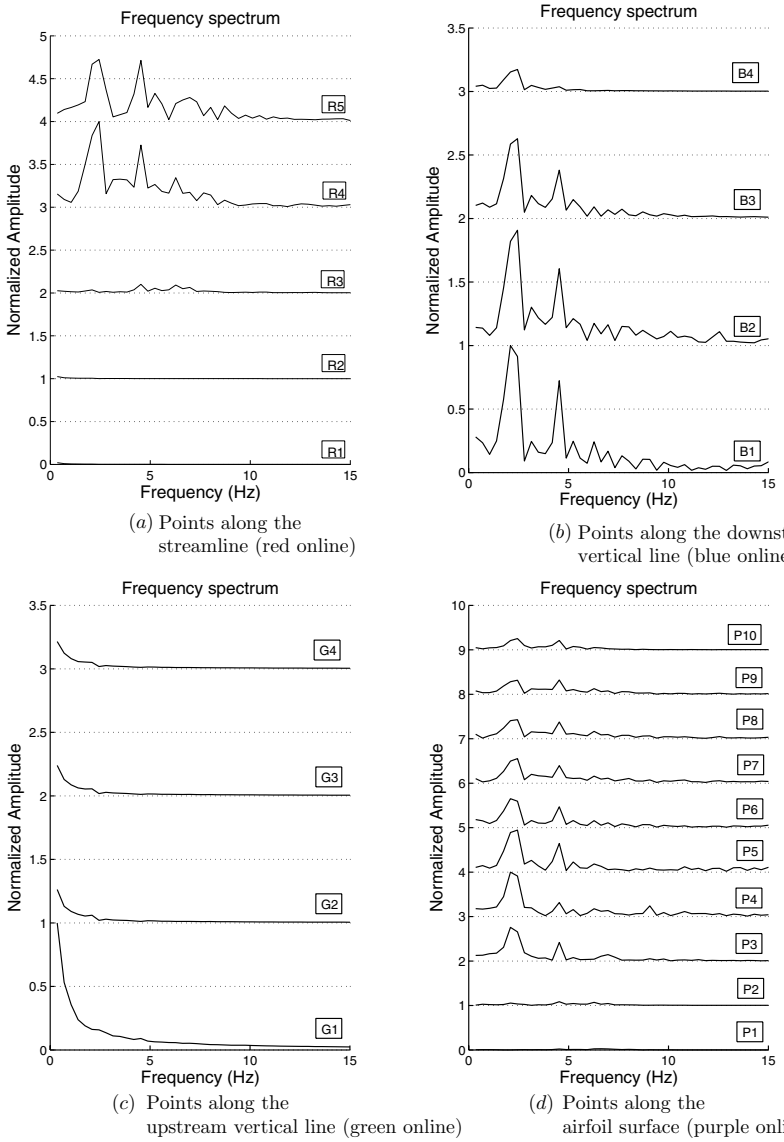

(*a*) Points along the streamline (red online)

(*b*) Points along the downstream vertical line (blue online)

(*c*) Points along the upstream vertical line (green online)

(*d*) Points along the airfoil surface (purple online)

Figure 24. Frequency spectra for the points shown in figure 19. Each group (red, green, blue and purple in the online version) has been normalized by the maximum amplitude occurring in this group.

(blue online) points, figure 23, we see large variations in the flow velocity because we are now looking at the wake region, figure 23. Interestingly, if we compare all 24 points, we find only three phase plots (R4, R5 and B2) which have larger fluctuations in the vertical velocity than the horizontal velocity. These points all lie on or near the streamline in the vortex wake region. This is indicative of the vortex formation and roll-up process that we have illustrated throughout this paper.

The phase analysis presented here provides several interesting incites. First, points in the vortex formation and wake region can be expected to exhibit highly periodic behavior with a

dominant frequency matching that of the vortex shedding and a strong secondary frequency of twice this value. The phase plots for the points along the airfoil surface (figure 21) readily demonstrate the presence of a secondary harmonic by the 'knots' seen in the phase plots, but a frequency spectrum analysis reveals that this secondary harmonic is present in almost all points downstream of P3. As discussed by Xilin *et al* [23], the presence of the subharmonic characterizes this flow as having vortex pairing and roll up, exactly as we have seen in our analysis using coherent structures. We attribute the absence of the secondary frequency at B4 to the distance of B4 from the airfoil surface. The roll-up process does not reach this point so only the primary frequency appears. Finally, flow actuation techniques may be able to take advantage of the highly periodic nature of the flow in the vortex shedding region by identifying key times for actuation.

7. Conclusion

In this study we have investigated the flow topology for low Reynolds number, unsteady flow behind an airfoil. We have provided a comprehensive study of the flow behavior in physical space and phase space, and seen good agreement between all areas of flow analysis. We have documented the evolution of the invariant manifolds during vortex shedding and observed the time-dependent motion of the reattachment profile. We have found that the reattachment profile periodically develops and propagates downstream to be shed with a vortex as a new reattachment profile forms upstream. The invariant manifolds also allow the identification of individual vortices which pair together and form a larger vortex which will be shed from the airfoil. The flow topology and motion of the fixed points are also examined. We find for vortex shedding what others have seen in a number of flows, that the motion of fixed points is related to the behavior of invariant manifolds. Finally, the phase plot behavior of a number of representative points is examined. It is noted that the velocity phase plot behavior in the shedding region is highly periodic. Knowing this, it is suggested that this velocity pattern can be used as a flow control feedback mechanism to identify the current stage of vortex shedding. The end result of this investigation is an improved picture of the vortex shedding process, one which may lead to further insights.

Acknowledgments

The authors would like to acknowledge the support for this investigation through an AFOSR grant from Computational Mathematics group managed by Dr F Fahroo. The authors would also like to acknowledge the developers of ManGen, Francois Lekien and Chad Coulliette [24], and Shawn Shadden [8].

References

[1] Hornton H P 1968 Laminar separation bubbles in two and three-dimensional incompressible flow *PhD Thesis* University of London

[2] Abbot D E and Kline S J 1962 Experimental investigations of subsonic turbulent flow over single and double backward-facing steps *Trans. ASME* D **84** 317–25

[3] Goldstein R J, Eriksen V L, Olson R M and Eckert E R G 1970 Laminar separation, reattachment, and transition of the flow over a downstream-facing step *Trans. ASME* D **92** 732–41

[4] Pauley L, Moin P and Reynolds W C 1990 The structure of two-dimensional separation *J. Fluid Mech.* **220** 397–411

[5] O'Meara M M and Mueller T J 1987 Laminar separation bubble characteristics on an airfoil at low Reynolds numbers *AIAA J.* **25** 1033–41

[6] Muti Lin J C and Pauley L L 1996 Low-Reynolds-number separation on an airfoil *AIAA J.* **34** 1570–7
[7] Yuan W, Xu H, Khalid M and Rasespiel R 2006 A parametric study of LES on laminar-turbulent transitional flows past an airfoil *Int. J. Comput. Fluid Dyn.* **20** 45–54
[8] Shadden S C, Lekien F and Marsden J E 2005 Definition and properties of Lagrangian coherent structures from finite-time Lyapunov exponents in two-dimensional aperiodic flows *Physica* D **212** 271–304
[9] Rom-Kedar V and Wiggins S 1990 Transport in two-dimensional maps *Arch. Ration. Mech. Anal.* **109** 239–98
[10] Hall J 2007 Low Reynolds number aerodynamics for Micro Aerial Vehicles *Master's Thesis* University of Colorado (Boulder, CO)
[11] Haller G 2002 Lagrangian coherent structures from approximate velocity data *Phys. Fluids* **14** 1851–61
[12] Haller G and Yuan G 2000 Lagrangian coherent structures and mixing in two-dimensional turbulence *Physica* D **147** 352–70
[13] Boffetta G, Lacorata G, Redaelli G and Vulpiani A 2001 Detecting barriers to transport: a review of different techniques *Physica* D **159** 58–70
[14] Sahin M, Hall J, Mohseni K and Hillewaert K 2008 Direct numerical simulation of separated low-Reynolds number flows around an Eppler 387 airfoil (AIAA paper AIAA 2008-0422, Reno, NV, 7–10 Jan. 2008) *46th AIAA Aerospace Sciences Meeting and Exhibit*
[15] Gyllhem D, Mohseni K, Lawrence D and Geuzaine P 2005 Numerical simulation of flow around the Colorado micro aerial vehicle (AIAA paper 2005-4757, American Institute of Aeronautics and Astronautics) *35th AIAA Fluid Dynamics Conf. and Exhibit* (Toronto, Canada, 6–9 June)
[16] Mueller T J 1999 Aerodynamic measurements at low Reynolds numbers for fixed wing micro-air vehicles *Development and Operation of UAVs for Military and Civil Applications* (VKI, Belgium, Sept. 13–17)
[17] Bonet J and Peraire J 1990 An alternating digital tree (adt) algorithm for 3d geometric searching and intersection problems *Int. J. Numer. Methods Eng.* **31** 1–17
[18] Haller G 2004 Exact theory of unsteady separation for two-dimensional flows *J. Fluid Mech.* **512** 257–311
[19] Inanc T, Shadden S C and Marsden J E 2005 Optimal trajectory generation in ocean flows *American Control Conf.* pp 674–9
[20] Cardwell B and Mohseni K 2008 Vortex shedding over two-dimensional airfoil: where do the particles come from? *AIAA J.* **46** 545–7
[21] Shadden S C, Dabiri J O and Marsden J E 2006 Lagrangian analysis of fluid transport in empirical vortex ring flows *Phys. Fluids* **18** 047105–1
[22] Hunt J C R, Abell C J, Peterka J A and Woo H 1978 Kinematical studies of the flows around free or surface-mounted obstacles; applying topology to flow visualization *J. Fluid Mech.* **86** 179–200
[23] Xilin X, Weiwei M and Huiliang Z 2003 Coherent structures in countercurrent axisymmetric shear flows *Acta Mech. Sin.* **19** 11–32
[24] Lekien F, Coulliette C, Mariano A J, Ryan E H, Shay L K, Haller G and Marsden J E 2005 Pollution release tied to invariant manifolds: a case study for the coast of Florida *Physica* D **210** 1–20